Article

Flexible intelligent microwave metasurface with shape-guided adaptive programming

Fan Li [1], Taisong Pan [1] ✉, Weihan Li [2], Zujun Peng[3], Dengji Guo[1], Xiang Jia[1], Taiqi Hu[1], Lingxiao Wang[4], Wei Wang[3], Min Gao [1], Guang Yao [1], Le Zuo[5], Mei Bi[1], Xiaolong Weng[4], Wenxuan Tang [2] ✉ & Yuan Lin [1,6,7] ✉

Empowering the reconfigurable metasurfaces (RM) with the capability to be mechanically deformable highlights the possibility to manipulate the electromagnetic (EM) wave across arbitrary surfaces. Such ambition is hampered by the absence of adaptivity to shape variation in current programming strategies for RM. Herein, we present a flexible intelligent surface platform (FISP) as a solution to achieve flexible RM with highly stable performance under dynamic deformation. The geometry acquisition module in FISP enables real-time awareness of RM's deformation with the conformal sensor array. By merging the actual shape of flexible RM into the input of the adaptive algorithm driven by the artificial neural network, the deformed flexible RM in FISP can be autonomously encoded by the bias voltage supply module to ensure robust performance under various deformation conditions. The versatility of FISP in manipulating EM waves is demonstrated by its applications in electromagnetic illusion, carpet cloaking, and data transmission, illustrating the prospects for seamlessly integrating flexible electronics and RM in the development of future EM metasurfaces.

Reconfigurable metasurface (RM)[1–4], which is distinguished by its capability to freely manipulate electromagnetic (EM) wave[5–13], has been a transformative platform for diverse applications such as non-line-of-sight (NLOS) communications[14–18], cloaking[19,20] and EM illusion[21–23]. Despite significant advancements, achieving RM functionality across arbitrary geometries remains a critical challenge in the pursuit of a universal and ubiquitous EM regulation scheme. The compatibility of RM with arbitrary geometries involves two essential aspects: the mechanical flexibility for shape transformation and the performance adaptability to varying geometries. In terms of the mechanical flexibility of RM, the development of flexible electronics has shown the feasibility of creating flexible RMs capable of conforming to different geometries through their own deformation[24–26]. However, there is still

plenty of room for the performance adaptivity of the RM with the mechanical deformation. Since the EM characteristics of meta-atoms in RM, such as phase and coupling strength, significantly depend on the shape of RM[24,27], adequate programming of RM with the undergoing deformation condition is critical for RM to perform with designed properties. For current RMs with customized shapes, their performance adaptivity to deformation is still restricted to specific deformation conditions[28–32], thereby restricting their applicability in scenarios with dynamic and non-deterministic deformations, such as those involving aerodynamic loading and environmental disturbance.

The key to address such challenges is to bridge the gap between the shape deformation and the programming strategy for flexible RM. While the RM can realize dynamic reconfiguration of EM

[1]School of Materials and Energy, University of Electronic Science and Technology of China, Chengdu, China. [2]State Key Laboratory of Millimeter Waves and Institute of Electromagnetic Space, Southeast University, Nanjing, China. [3]Institute of Flexible Electronics Technology of THU, Jiaxing, China. [4]School of Electronic Science and Engineering, University of Electronic Science and Technology of China, Chengdu, China. [5]The 29th Research Institute of China Electronics Technology Group Corporation, Chengdu, China. [6]State Key Laboratory of Electronic Thin Films and Integrated Devices, University of Electronic Science and Technology of China, Chengdu, China. [7]Medico-Engineering Cooperation on Applied Medicine Research Center, University of Electronic Science and Technology of China, Chengdu, China. ✉e-mail: tspan@uestc.edu.cn; wenxuant@seu.edu.cn; linyuan@uestc.edu.cn
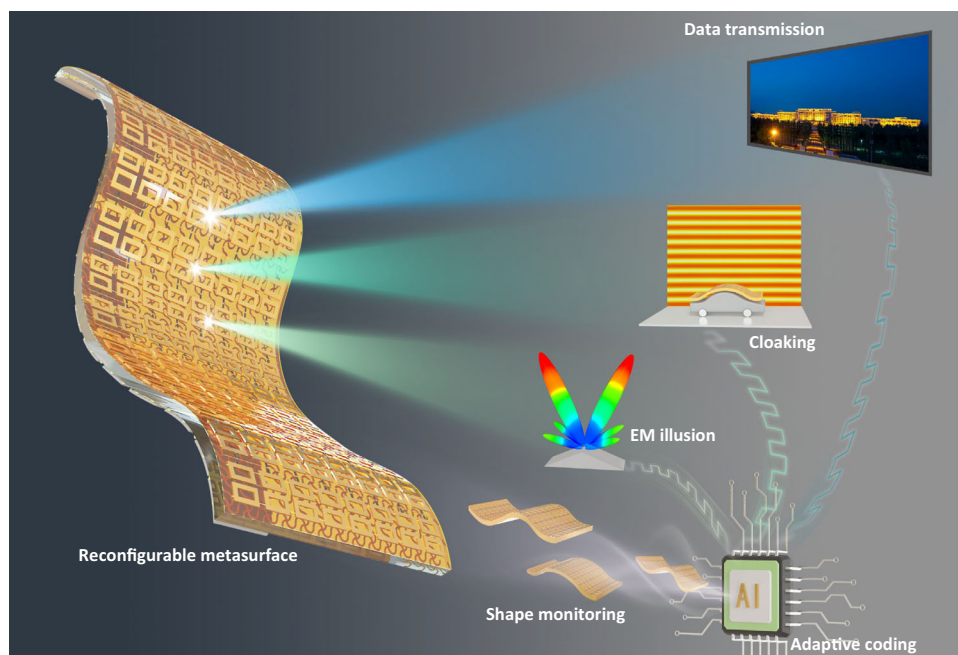
Fig. 1 | Schematic illustration of the flexible intelligent surface platform (FISP). This platform is realized through the combination of a flexible reconfigurable metasurface, a geometry acquisition module (GAM), and a bias voltage supply module (BSM). GAM enables the real-time shape monitoring of the reconfigurable metasurface. Transient shape information is fed to the BSM driven by ANN to adaptively determine the bias voltage for metasurface reconfiguration, which achieves the robustness of FISP to dynamic deformations. FISP can perform various functionalities, such as illusion, cloaking, and wireless data transmission.

characteristics with electrically tunable devices[33], current programming strategies fail to account for the impact of deformation on RM's performance. The incorporation of shape-related elements in the encoding of RM is expected to enable flexible RM with performance adaptivity to arbitrary deformations. Recent advances in the adaptive programming of RM offer a promising pathway to achieve this goal by exploiting the neural network (NN) algorithms[34,35]. NN-driven algorithms facilitate efficient programming of RM without time-consuming simulations, enabling applications such as complicated scattering patterns[36–41], self-adaptive microwave cloaking[20,42,43], and automatic target tracking[44,45]. Moreover, the emergence of flexible sensors that can conformally attach to the deformable RM makes it possible to let the RM to perceive their own deformation without interfering with RM's operation. These studies suggest the potential to create a self-adaptive flexible RM with performance robustness to the deformation by constructing a closed-loop system framework with the seamless integration of deformation sensors and NN-driven adaptive programming strategies.

In this study, we demonstrate a flexible intelligent surface platform (FISP) as a solution for microwave RM to achieve adaptive operation under time-varying deformations. The flexible RM features meta-atoms composed of symmetric square ring resonators (SRRs) and parallel varactor diodes, allowing precise control over the reflection phase of each meta-atom. We also propose a mesh layout for RM's ground plane to ensure the mechanical flexibility of RM. The geometry acquisition module in FISP enables real-time monitoring of RM's shape by assessing the local bending radius of RM with the flexible sensor array conformally attached to the RM. Leveraging a pre-trained artificial neural network (ANN), we develop the algorithm to utilize the shape information to adaptively program the RM. With the feeding of the data from the sensor array, the ANN-driven algorithm generates the coding sequence to stabilize RM performance with a response time of approximately 16.7 ms. Based on FISP, we demonstrate three representative applications of FISP, including EM illusion, conformal cloaking, and data transmission. FISP exhibits significant robustness against arbitrary bending deformations in these applications, illustrating its versatility and reliability in practical scenarios.

Results
Framework of FISP
As illustrated in Fig. 1, FISP consists of three primary components: the flexible reconfigurable metasurface (flexible RM), the geometry acquisition module (GAM), and the bias voltage supply module (BSM). The flexible RM enables the dynamic alteration of metasurface's EM characteristics, which lays the foundation for manipulating EM waves. The GAM monitors the shape of the flexible RM in real-time and provides RM's deformation condition to the BSM. With the guidance of the data fed by the GAM, the BSM computes the phase offset matrix for the meta-atoms in flexible RM, which is delivered to an ANN-driven algorithm within the BSM. This algorithm subsequently determines the coding sequence and programs the flexible RM to mitigate the performance deviations caused by deformation. By ensuring stable performance under dynamic deformations, FISP provides a versatile platform for various applications. In this study, we demonstrate three specific applications of FISP. First, FISP facilitates EM illusion in the scenario involving conformal integration, achieving consistent illusions across various deformation conditions. Second, FISP is programmed as a flexible carpet cloak to effectively conceal the target objects. FISP shows a total radar cross-section (RCS) reduction of no less than -77% with the deformation of the flexible RM. Additionally, FISP serves as a flexible, adaptive reflectarray antenna. The antenna maintains a stable beam direction when the flexible RM undergoes dynamic deformation, empowering highly adaptive video data transmission with a stable error vector magnitude (EVM) of -20 dB.

Design of the flexible reconfigurable metasurface
In this study, we design a reflective flexible RM as a specific example of the RM within the FISP framework. As illustrated in Fig. 2a, the flexible RM features a three-layer structure composed of metallic meta-atoms on a polyimide (PI) film, polydimethylsiloxane (PDMS) substrate, and a ground plane formed by a metallic mesh (see Methods section for
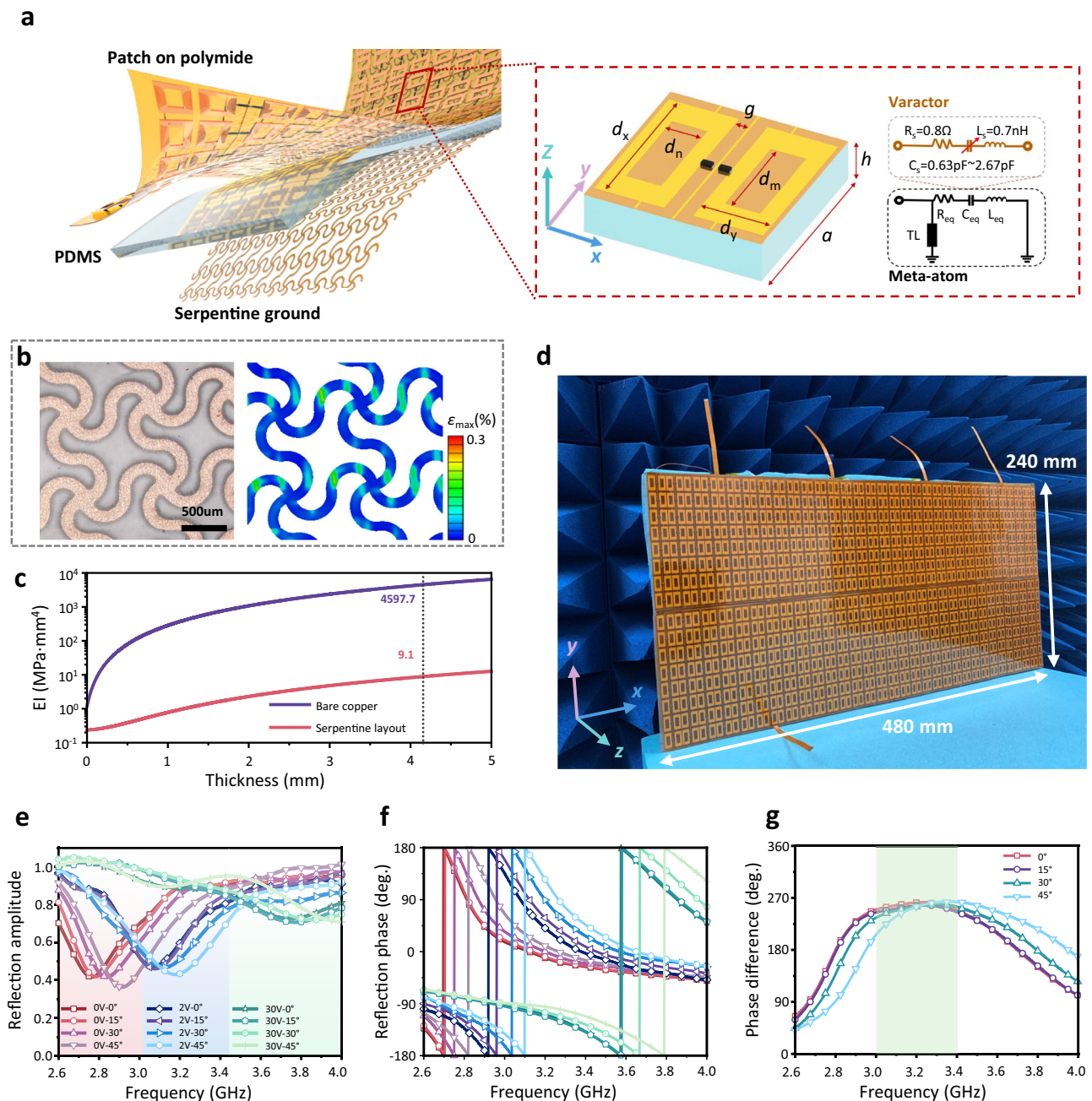
Fig. 2 | Design of flexible reconfigurable metasurface. a Exploded view of RM and the structure of meta-atom. **b** Photograph and simulation result of strain distribution showing the serpentine traces in the ground plane when it bent with a bending radius of 50 mm. **c** Comparison of the bending stiffness of the RMs with the ground planes based on bare copper and serpentine layout. **d** Photograph of fabricated RM. Measured (**e**) reflection magnitude and (**f**) phase of meta-atoms with varying varactor capacitance and angle of incidence. The color lines in the two panels correspond to the same capacitance of varactor and angle of incidence. **g** Measured dependence of phase variation on frequency with varying angles of incidence.

geometric parameters). The meta-atom in the RM incorporates symmetric SRRs paired with parallel varactor diodes. The use of parallel varactor diodes enables continuous phase regulation over a wide range by adjusting the bias voltage, thereby achieving arbitrary reflection phase offset (0–2π) within the proposed flexible RM (see Supplementary Note 1 for details on meta-atom design). The ground plane of RM plays a crucial role in confining the EM field and enhancing reflection efficiency. Typically, ground plane is constructed from metal plates, which is unfavorable for achieving the mechanical flexibility of the RM. As shown in Fig. 2b, we utilize a serpentine mesh layout to create the ground plane of flexible RM (see Supplementary Note 2 for the details of ground plane design). The open cavities in the mesh

ground plane significantly reduce the bending stiffness of RM, making it easier to warp under mechanical loading (Supplementary Fig. 5c). The high fill factor and excellent electrical conductivity of metallic serpentine mesh structure also benefit the EM performance of RM. The bending stiffness estimation presented in Fig. 2c further validates the effectiveness of mesh design. Specifically, the bending stiffness of the flexible RM decreases by more than two orders of magnitude when using a mesh ground plane to replace a bare copper plate (see Supplementary Note 3 for details of bending stiffness assessment). As illustrated in Fig. 2d, the dimension of RM is 480 × 240 mm² (32 × 16 meta-atoms), with an identical bias voltage applied to the meta-atoms in the same column along the y-direction.

To validate the RM's design, we measure the reflection characteristics of the undeformed flexible RM at frequencies ranging from 2.6 GHz to 4 GHz. Figure 2e illustrates the amplitude response of the reflected wave with varying bias voltages and angles of incidence (AOIs). As the capacitance of the varactor increases (from 0.63 pF to 2.67 pF) with a decrease in bias voltage (from 30 V to 0 V), a blue shift in resonant frequency is observed. Notably, the normalized reflection amplitude remains above 0.4 with all combinations of bias voltage and AOI, ensuring sufficient reflection efficiency within this frequency range. The phase response of the reflected wave shown in Fig. 2f confirms the feasibility to program the phase characteristics of the flexible RM with appropriate bias voltage configurations. Based on the measured phase response, we also extract the phase modulation range of the flexible RM, which is shown in Fig. 2g. Within the frequency range of 3.0 GHz to 3.4 GHz, the phase of the reflected wave can be tuned up to 270° with the AOIs ranging from 0° to 45°. Consequently, the operation band of the flexible RM in FISP is determined to be in the frequency band of 3.0 GHz to 3.4 GHz.

Adaptive programming in FISP

The adaptive programming of FISP involves perceiving the shape of flexible RM using the GAM and generating the corresponding coding sequence with the BSM. The underlying principle of the GAM is based on approximating discrete circular segments to form a continuous geometry. Given that each column of the meta-atoms in RM shares the same bias voltage, the RM can be considered as a set of arc nodes with identical arc length (a) but varying bending radii. As illustrated in Fig. 3a, the shape of RM can be reconstructed by sequentially connecting the circular segments (arcs) once the AOI and the location of each arc are determined. Upon deformation, the AOI of the nth column of meta-atoms (φ_n) can be calculated with its bending radius (r_n):

$$\varphi_n = \sum_{i=1}^{n} \left(\frac{a}{r_{i-1}} + \frac{a}{2r_i} \right), \tag{1}$$

The corresponding location of the nth column along the length direction (Y_n) can be then derived from the AOI and the bending radius:

$$Y_n = Y_1 + \sum_{i=1}^{n} \left[(r_{i-1} - r_i) \times \cos\left(\varphi_n - \frac{a}{2r_n} \right) \right] + r_n \times \cos(\varphi_n), \tag{2}$$

where Y_1 represents the location of the first column (the column at the edge of the flexible RM). Since the tensile deformation is negligible, the change in the location of meta-atoms in width direction can be ignored. Therefore, the shape of the flexible RM can be reconstructed with the result of Eq. 2.

The above discussion indicates that the bending radius of each arc node is the key factor for assessing the deformation of the flexible RM. In FISP, we achieve the real-time monitoring of bending radius by incorporating a linear array of flexible strain sensors in the GAM. As shown in Fig. 3b, the sensors are conformally integrated on the backside of the RM. Each sensor corresponds to a column of the meta-atoms (32 sensors for 32 columns of meta-atoms). The sensor transduces the bending strain into resistance variation, from which the bending radius is further derived (see Supplementary Note 4 for the principles of the GAM). Figure 3c compares the shapes of the RM obtained by the GAM and binocular stereo camera. The results demonstrate excellent consistency across nine deformation conditions. The shape discrepancies between these two methods are quantified by the root-mean-square deviation (RMSD), as illustrated in Fig. 3d and detailed in Supplementary Note 4. The RMSD of the shape reconstructed by the GAM is as low as 2.36 mm when the maximum displacement reaches 45 mm from the reference plane.

Realizing the acquisition of RM's shape with the GAM paves the way to guide the programming of RM with the immediate shape change. When FISP performs with specific functionality, a functionality phase (F_n) is pre-designed for each column of meta-atoms using full-wave simulations or analytical calculations. Then, the desired phase (P_n) for a given deformation condition can be obtained:

$$P_n = F_n + \left(\pi - 4 \times \pi \times Y_n \times \frac{\cos(\varphi_n)}{\lambda} \right), \tag{3}$$

where λ represents the wavelength of the operating frequency. Supplementary Fig. 9 also presents a schematic diagram of the calculation process. While Eq. 3 establishes a foundation for programming the RM, the corresponding bias voltages of the meta-atoms are difficult to be directly extracted from the phase matrix. Therefore, we employ a pretrained ANN within the BSM to derive the bias voltage configuration to achieve the adaptive encoding of RM without human intervention. The model is a fully connected ANN formed by 6 hidden layers and 60 neurons per layer. As depicted in Fig. 3e, the inputs of the ANN include absolute AOI matrix (θ_n), operating frequency (f), and desired phase matrix (P_n). The absolute AOI matrix and desired phase matrix are calculated using Eqs. 1 and 3, respectively. The bias voltage configuration for 32 columns of meta-atoms is then obtained as the output of the ANN. The ANN is trained using a normalized dataset obtained by experimental measurements using the proposed flexible RM. The dataset contains 190,000 reflection phase values, covering a wide range of frequencies, AOIs, and bias voltages (see Methods section for the measurement setup of the reflection spectrum). To balance the cost and loss of the ANN training, the dataset is split into 67% training data and 33% test data (Supplementary Note 5 for details of the BSM design). The loss of the test set shown in Fig. 3f is as low as 0.015, indicating smooth ANN performance without significant overfitting.

The ANN-driven control program, combined with the bias voltage supply unit and the control board based on a field-programmable gate array (FPGA), forms the backbone of the BSM. The multiple output channels in FPGA are capable of independently transmitting the configuration of bias voltage to the varactors in the meta-atoms of each column (Supplementary Note 5). As demonstrated by Fig. 3g, we also evaluate the response time for a single reconfiguration process (from shape acquisition to bias voltage supply). The experimental setup for verification is outlined in Supplementary Note 6. The data preparation time for ANN inputs is 4 ms, comprising ~2 ms for data reception (at a sampling rate of ~1200 Hz per GAM channel) and ~2 ms for processing. The inference time of ANN for 32 bias voltage channels is nearly 2 ms. The measured response time of the power supply module is 5.25 ms, and the switching time of the varactor is negligibly short. However, due to the transmission rate limitation of the RS-232 protocol, the measured response time for the entire process of our FISP system is 16.76 ms, which is approximately 5.5 ms slower than the response time obtained from theoretical analysis. (see Supplementary Note 6 for details of the assessment of response time in FISP).

Proof-of-concept demonstrations of FISP

The applications of FISP are demonstrated in three scenarios: EM illusion, carpet cloak, and reflectarray antenna. In the demonstrations, the mechanical loadings are applied to RM with a custom-built mechanical platform (Supplementary Note 7). The near-field and far-field measurements are conducted in an anechoic chamber. The experimental setups are depicted in Fig. 3h and Supplementary Fig. 15b. Under the normal incidence of a perpendicularly polarized Gaussian beam at the operating frequency of 3.1 GHz and 3.3 GHz, where the magnetic field is perpendicular to the current direction in the varactors, FISP demonstrates its capability to generate expected EM illusions under different deformation conditions. The near-field distribution of the flat illusions, corresponding to six deformation
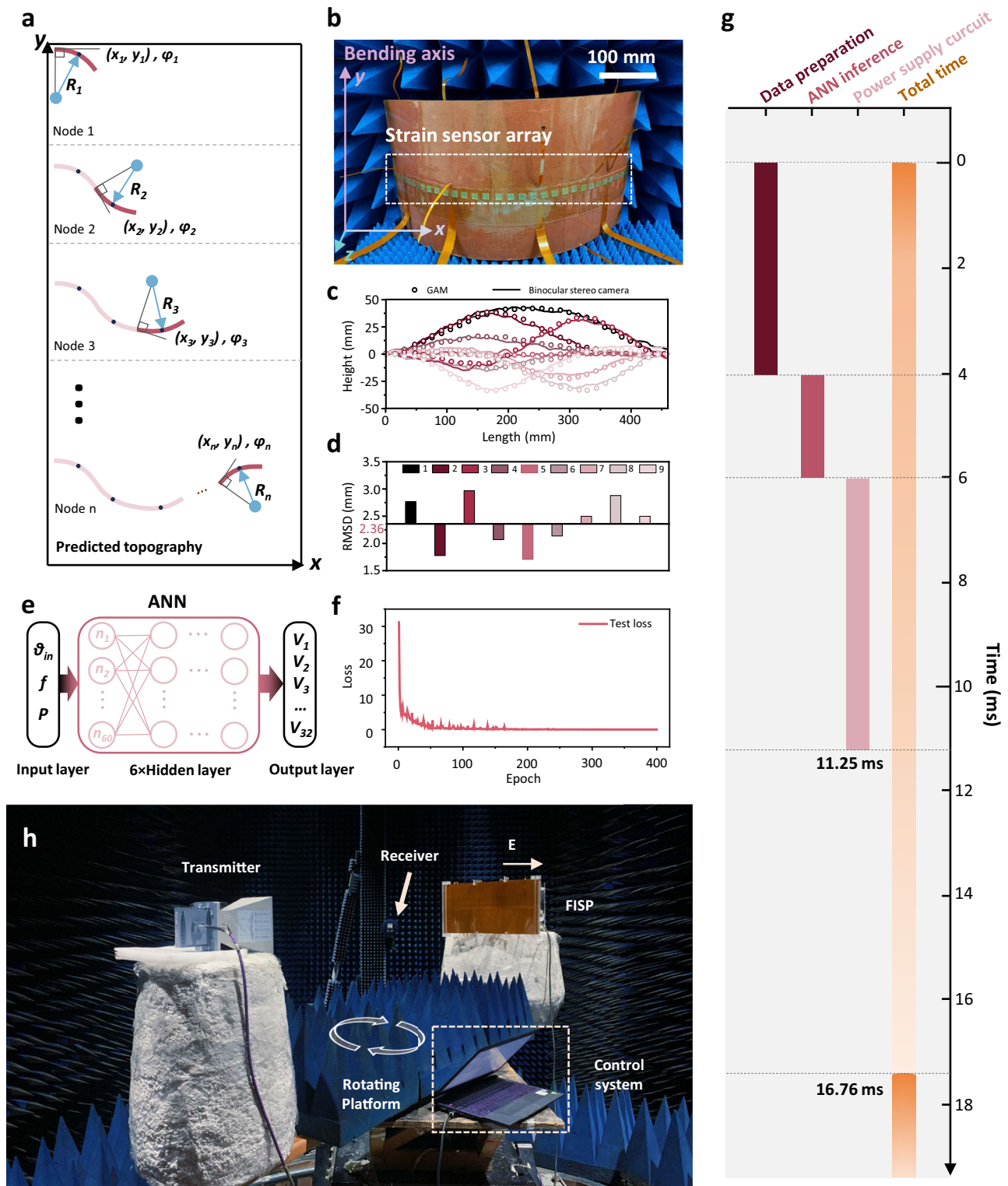
Fig. 3 | Adaptive programming and verification setup. a Principle of shape assessment with the GAM. **b** Arrangement of sensors on the bottom surface of RM. **c** Comparison of the RM's shapes captured by the GAM and binocular stereo camera. **d** Root-mean-square deviation (RMSD) values of the GAM-monitored shape when using the camera-measured result as reference. **e** Structure of the ANN model in BSM. **f** Test loss of the ANN over the epoch. **g** Time evolution of the adaptive programming operation. **h** Experiment setup for far-field measurement.

conditions (shapes 1-6), are shown in Fig. 4a and Supplementary Fig. 16a. The reflected magnetic field of flexible RM remains analogous to the horizontal wavefront when the RM undergoes deformation. We also investigate the EM illusion performance with oblique and triangular illusions at a tilt angle of 15°. As demonstrated in Fig. 4b, c, and

Supplementary Fig. 16b, c, single or dual beams with the intended reflection angle of 30° are also realized with the changing shapes of RM and a 2° margin of error. Polar plots of far-field scattering patterns, illustrated in Fig. 4d–f and Supplementary Fig. S16d–S16f, further verify the ability of FISP to maintain distinct scattering peaks at 0°, 30°,
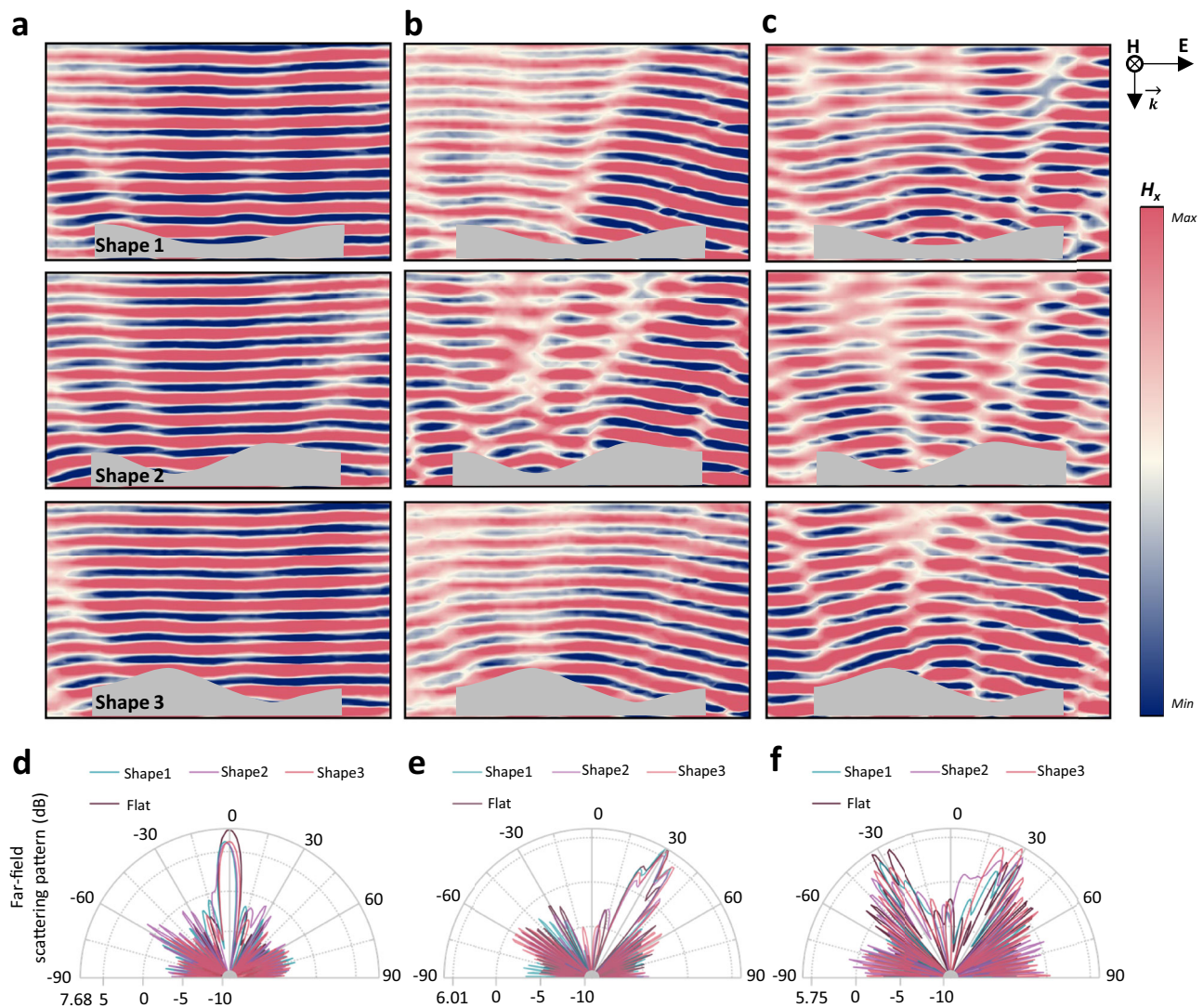
Fig. 4 | Experimental demonstration of illusions with FISP. Near-field distribution of magnetic field (H_x) in (**a**) flat illusion, (**b**) oblique illusion, and (**c**) triangular illusion with a tilt angle of 15° and varying RM shapes. Corresponding polar plots of the far-field patterns of (**d**) plane illusion, (**e**) oblique illusion, and (**f**) triangular illusion. All the measurements are taken at normal incidence and 3.1 GHz.

and ±30° with different deformation conditions. In contrast, the near-field characteristics of the flexible RM significantly deteriorate without utilizing the GAM and the BSM (Supplementary Fig. 17).

The capability of FISP to function as a carpet cloak is demonstrated using a car-shaped model as the cloaked object against backgrounds with two different geometries (background 1 and background 2 in Fig. 5). In the demonstrations, FISP operates at the frequencies of 3.1 GHz and 3.3 GHz. Figure 5a shows the experimental scenarios and corresponding results of the scattering field distributions. When the flexible RM deforms across various shapes, FISP always recovers the scattering field distributions with the existence of a car-shaped model to the ones with backgrounds only. Meanwhile, significant deviations are observed in the cases without activating the GAM and the BSM. The total differential RCS results of the cloaked scenarios are reduced by at least 76.86% compared with the bare object, as shown in Fig. 5b, c. The cloaking results at different operating frequencies are also presented in Supplementary Fig. 19, and the experimental details are outlined in Supplementary Note 8.

FISP also shows great potential as a flexible reflectarray antenna with robust performance under dynamic deformation. As shown in Fig. 6a, performance degradation may be caused by the flutter of aerofoils when the flexible reflectarray antenna is conformally mounted on the aircraft, due to the impacts of inertial force, aerodynamic force, and elastic force of the structure. Figure 6b and Supplementary Fig. 20a show the experimental setup for wireless communication with FISP mounted on an aerofoil model. The receiver is positioned at either a normal (0°) or oblique (30°) angle at a distance of 2 m from the flexible RM. Real-time video streaming at 3.1 GHz is used to evaluate the wireless communication performance, accompanied by the received constellation diagram and error vector magnitude (EVM) of the quadrature phase shift keying (QPSK) scheme for quantitative analysis. As illustrated in Fig. 6c and Supplementary Fig. 20b, continuous video streaming is maintained during deformation. The received constellation diagram also remains stable in the demonstration, contrasting sharply with the erratic performance observed in the absence of self-adaptive programming (Fig. 6d and Supplementary Fig. 20c). The EVM value obtained, which keeps being around −20 dB with deformed RM, indicates the stable and high quality of the transmitted QPSK signal (Fig. 6e and Supplementary Fig. 20d). Supplementary Movies 1-4 further highlight the uninterrupted video streaming empowered by FISP.

The reflectarray antenna based on FISP even shows robust wireless communication performance with more complex deformation
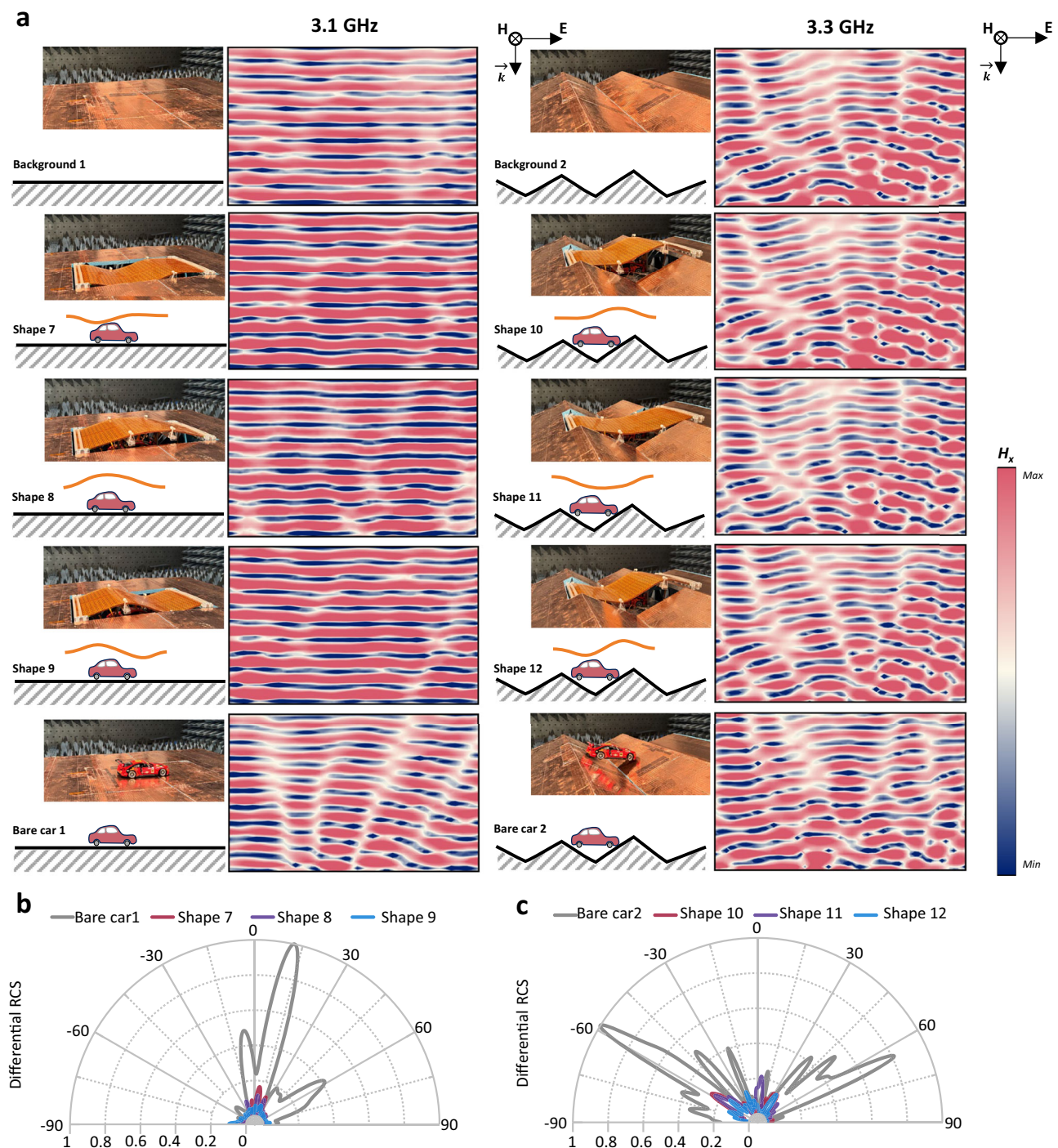
Fig. 5 | Experimental demonstration of carpet cloak with FISP. a Schematics of measurement scenarios (background, with deformed RM, and barely cloaked object with background), and corresponding Near-field magnetic field (**H**$_x$) distributions. A car-shaped model is used as the cloaked object. Differential RCS reduction results of different measurement scenarios when comparing with the (**b**) flat (3.1 GHz) and (**c**) zigzag (3.3 GHz) backgrounds.

conditions. With the experimental setups shown in Supplementary Fig. 21a and c, the mechanical loadings are simultaneously applied to two positions on the flexible RM. Supplementary Fig. 21b and d illustrate the captured video frames at 3.1 GHz in both the normal and oblique setups with various deformation shapes. The transmission coefficient (S$_{21}$) of RM in FISP barely changes, as shown in Supplementary Fig. 22. The corresponding results are also demonstrated by Supplementary Movies 5–10. Moreover, we also demonstrate the high tolerance of FISP to arbitrary deformation. As demonstrated in Supplementary Movies 11 and 12, the stable video streaming is also

achieved when applying random mechanical loadings to the flexible RM.

Discussion

We propose and demonstrate the flexible intelligent surface platform (FISP) that enables the adaptive programming of RM under dynamic deformation. By utilizing a flexible strain sensor array integrated with the flexible RM, real-time monitoring of the shape of RM is achieved. The transient shape information is processed by an ANN-driven algorithm, which enables the adaptive encoding of the RM to ensure high-
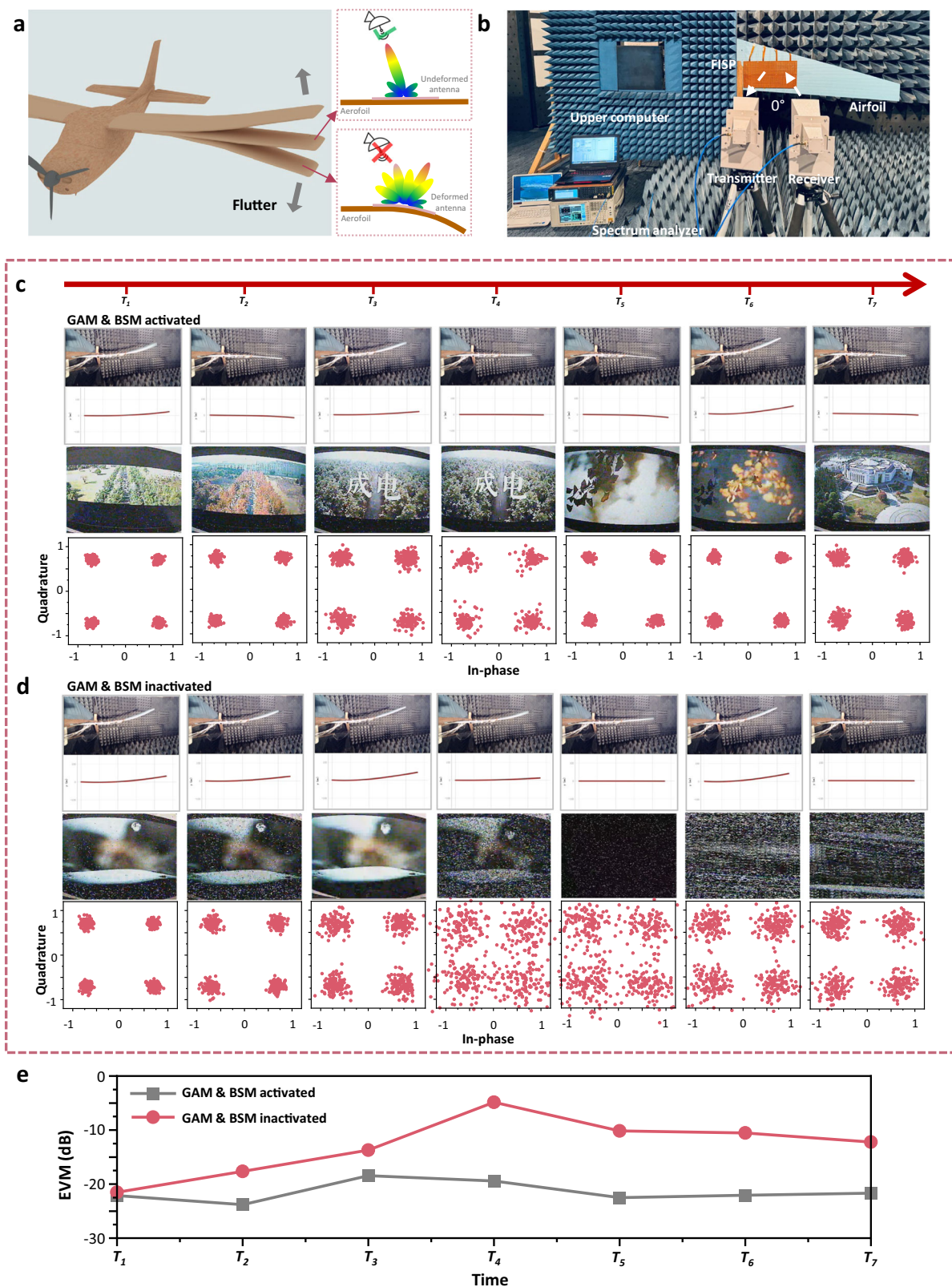
Fig. 6 | Experimental demonstration of reflectarray antenna with FISP.
a Schematic of the performance degradation of the flexible reflectarray antenna with aerofoil flutter. **b** Experimental setup for video streaming when the receive antenna is placed at normal setup (beam direction of 0°). Experiment results of the captured real-time video frames and constellation diagrams with seven transient shapes when the GAM and the BSM are (**c**) activated or (**d**) inactivated. **e** Corresponding error vector magnitudes of the received signal for the seven transient shapes.

performance robustness to dynamic deformation. The proof-of-concept applications, including illusion, cloaking, and data transmission, validate FISP's versatility as a universal platform for EM wave manipulation. FISP alters the current shape-by-shape design strategy for flexible reconfigurable metasurface by introducing a shape-guided, self-adaptive, and closed-loop programming strategy to realize high-performance robustness to deformation. FISP also has the potential to be applied in scenarios with two-dimensional deformation (Supplementary Note 9). FISP is expected to pave the way for highly deployable intelligent RM and holds significant potential for next-generation intelligent wireless systems.

Methods

Geometric parameters of the meta-atom in RM
The meta-atoms in the RM were arranged with a of 15 mm period (parameter a in Fig. 2a), approximately 1/7 of the free-space wavelength at the operating frequency. Two symmetrical hollow rectangular patches were connected by two SMV1405-079LF varactor diodes, as shown in the SPICE model in the inset of Fig. 2a. The varactor diode capacitance was tunable between 0.63 pF and 2.67 pF via a reverse bias voltage range of 0–30 V. The meta-atoms and ground plane of RM were fabricated using 0.018-mm-thick copper foil. The other parameters shown in Fig. 2a were set to $g = 2.3$ mm, $d_x = 13$ mm, $d_y = 5.95$ mm, $d_m = 8$ mm, and $d_n = 3$ mm. The PDMS substrate had a thickness of 4.2 mm, a dielectric constant of 2.5, and a loss tangent of 0.03.

Fabrication of the RM
The resonant structure on the top surface was prepared by etching the 18-μm-thick copper foil laminated on 50-μm-thick PI film. Supplementary Fig. 5b shows the step-by-step schematic of the processes of ground plane fabrication and RM assembly. The ground plane was fabricated by patterning the copper-clad elastomer, which was produced by knife-coating the uncured 4.2-mm-thick PDMS on 18-μm-thick copper foil. The subsequent ultraviolet bonding treatment completed the assembly of RM by achieving the bonding of top resonant structure on the other side of PDMS substrate.

Fabrication of flexible sensor array
The fabrication started from preparing the interconnects in the array, in which the metallic patterns were realized using a standard flexible printed circuit (FPC) process and the serpentine-like shape of the interconnects was achieved by ultra-violet laser micromachining. The sensor units, each featuring a full Wheatstone bridge connection, were then soldered onto the interconnects. Each sensor unit was fabricated by patterning a 5-μm-thick Cu-Ni alloy thin film with dimensions of 10.5 mm × 9 mm. The sensitivity coefficient of the sensor unit was 2.11, with an initial (without mechanical loading) resistance of 1000 Ω. A 1-mm-thick layer of PDMS was utilized to encapsulate the sensor array after the soldering.

EM Simulations
Full wave simulations with Floquet port and unit cell boundary conditions were set up in CST Microwave studio to investigate the reflection spectra of the meta-atom. The varactor diode was modeled using a lumped element approach with equivalent RLC parameters of $R_s = 0.8$ Ω, $L_s = 0.7$ nH, $C_s = 0.63$–2.67 pF. The simulation covered a frequency sweeping range of 2.6 GHz to 4 GHz and an angle of incidence (AOI) range sweeping range of 0° to 45°.

Mechanical simulation
Commercial finite element analysis software (ABAQUS 2022) was employed in the simulations with a simplified model of the ground plane and PDMS substrate of the RM. The elastic modulus (E) and Poisson's ratio (v) of copper and PI were $E_{Cu} = 119$ GPa and $v_{Cu} = 0.35$ for

copper, and $E_{PI} = 2.5$ GPa and $v_{PI} = 0.34$ for PI, respectively. The PDMS substrate was modeled as a hyperelastic material, described by the Mooney–Rivlin constitutive model, with material coefficients of $C_{10} = 0.243243$, $C_{01} = 0.060811$, and $D_1 = 0.13333$.

Measurement setup
A binocular stereo camera was used to capture the reference shape of RM with an experimental setup shown in Supplementary Fig. 8. The experimental setup of free-space reflection spectrum measurement is shown in Supplementary Fig. 15a, in which the distance between the horn antennas and RM was set to fulfill the far-field conditions for generating a plane wave. To obtain the near-field distribution of magnetic field, a three-dimensional scanning platform with loop antenna was used to measure the amplitude of the reflected near-field scattering in step-scan mode, while another horn antenna serves as the transmitter antenna (Supplementary Fig. 15b). In the far-field tests, the transmitter horn antenna and RM were fixed on a support plate mounted on a rotating platform, which is capable of rotating from −90° to 90° in the horizontal plane (Fig. 3h). The differential RCS measurement was conducted on an angle-scanning platform, as shown in Supplementary Fig. 18. The distance between the horn antennas and RM was also set to fulfill the far-field conditions. In the reflectarray antenna tests, the transmitter antenna was positioned perpendicular to RM, while receiver antenna was positioned at a specific angle (0° and 30°) from the direction of incidence to continuously collect the reflected signal. The QPSK signal (3.1 GHz, 500 kbps, −10 dBm) was generated by vector signal generator (N5182B, Keysight). Signal analyzer (N9020A, Agilent) was used to demodulate the signal. S-parameters were obtained using a vector network analyzer (ZNB20, R&S).

Data availability
The main data supporting the findings of this study is contained within the main manuscript and its associated Supplementary Information. All other relevant data is available from the corresponding author upon request.

Code availability
The custom computer codes utilized during the current study are available from the corresponding authors on request.

References
1. Pendry, J. B., Schurig, D. & Smith, D. R. Controlling electromagnetic fields. *Science* **312**, 1780 (2006).
2. Chen, H. Y., Chan, C. T. & Sheng, P. Transformation optics and metamaterials. *Nat. Mater.* **9**, 387 (2010).
3. Yu, N. & Capasso, F. Flat optics with designer metasurfaces. *Nat. Mater.* **13**, 139 (2014).
4. Saifullah, Y., He, Y., Boag, A., Yang, G.-M. & Xu, F. Recent progress in reconfigurable and intelligent metasurfaces: a comprehensive review of tuning mechanisms, hardware designs, and applications. *Adv. Sci.* **9**, 2203747 (2022).
5. Chen, K. et al. A reconfigurable active huygens' metalens. *Adv. Mater.* **29**, 1606422 (2017).
6. Huang, C. et al. Reconfigurable metasurface for multifunctional control of electromagnetic waves. *Adv. Opt. Mater.* **5**, 1700485 (2017).
7. Li, L. et al. Electromagnetic reprogrammable coding-metasurface holograms. *Nat. Commun.* **8**, 197 (2017).
8. Ma, Q. et al. Smart metasurface with self-adaptively reprogrammable functions. *Light Sci. Appl.* **8**, 98 (2019).
9. Li, Y. et al. A tunable metasurface with switchable functionalities: from perfect transparency to perfect absorption. *Adv. Opt. Mater.* **8**, 1901548 (2020).

10. Abdollahramezani, S. et al. Electrically driven reprogrammable phase-change metasurface reaching 80% efficiency. *Nat. Commun.* **13**, 1696 (2022).

11. Hu, Q. et al. An intelligent programmable omni-metasurface. *Laser Photonics Rev.* **16**, 2100718 (2022).

12. Wei, M., Zhao, H., Galdi, V., Li, L. & Cui, T. J. Metasurface-enabled smart wireless attacks at the physical layer. *Nat. Electron.* **6**, 610 (2023).

13. Ning, J. et al. Reconfigurable tri-mode metasurface for broadband low observation, wide-Range tracing, and backscatter communication. *Adv. Sci.* **11**, 2304879 (2024).

14. Zhang, L. et al. A wireless communication scheme based on space- and frequency-division multiplexing using digital metasurfaces. *Nat. Electron.* **4**, 218 (2021).

15. Yildirim, I., Uyrus, A. & Basar, E. Modeling and analysis of reconfigurable intelligent surfaces for indoor and outdoor applications in future wireless networks. *IEEE Trans. Commun.* **69**, 1290 (2021).

16. Zhang, X. G. et al. A metasurface-based light-to-microwave transmitter for hybrid wireless communications. *Light-Sci. Appl.* **11**, 126 (2022).

17. Wang, S. R. et al. Manipulations of multi-frequency waves and signals via multi-partition asynchronous space-time-coding digital metasurface. *Nat. Commun.* **14**, 5377 (2023).

18. Rains, J. et al. High-resolution programmable scattering for wireless coverage enhancement: an indoor field trial campaign. *IEEE Trans. Antennas Propag.* **71**, 518 (2023).

19. Liu, S., Xu, H.-X., Zhang, H. C. & Cui, T. J. Tunable ultrathin mantle cloak via varactor-diode-loaded metasurface. *Opt. Express* **22**, 13403 (2014).

20. Qian, C. et al. Deep-learning-enabled self-adaptive microwave cloak without human intervention. *Nat. Photonics* **14**, 383 (2020).

21. Huang, C. et al. Reconfigurable metasurface cloak for dynamical electromagnetic illusions. *ACS Photonics* **5**, 1718 (2017).

22. Zhang, X. G. et al. An optically driven digital metasurface for programming electromagnetic functions. *Nat. Electron.* **3**, 165 (2020).

23. Liao, J. et al. Polarization-insensitive metasurface cloak for dynamic illusions with an electromagnetic transparent window. *ACS Appl. Mater. Interfaces* **15**, 16953 (2023).

24. Malek, S. C., Ee, H.-S. & Agarwal, R. Strain multiplexed metasurface holograms on a stretchable substrate. *Nano Lett.* **17**, 3641 (2017).

25. Zhang, C. et al. Stretchable all-Dielectric metasurfaces with polarization-insensitive and full-spectrum response. *ACS Nano* **14**, 1418 (2020).

26. Wang, C. X. et al. Pangolin-inspired stretchable, microwave-invisible metascale. *Adv. Mater.* **33**, 2102131 (2021).

27. Fan, X., Li, Y., Chen, S., Xing, Y. & Pan, T. Mechanical terahertz modulation by skin-like ultrathin stretchable metasurface. *Small* **16**, 2002484 (2020).

28. Xu, L. & Chen, H. Conformal transformation optics. *Nat. Photonics* **9**, 15 (2015).

29. Kamali, S. M., Arbabi, A., Arbabi, E., Horie, Y. & Faraon, A. Decoupling optical function and geometrical form using conformal flexible dielectric metasurfaces. *Nat. Commun.* **7**, 11618 (2016).

30. Wu, K., Coquet, P., Wang, Q. J. & Genevet, P. Modelling of free-form conformal metasurfaces. *Nat. Commun.* **9**, 3494 (2018).

31. Zhang, J., Shao, L., Li, Z., Zhang, C. & Zhu, W. Graphene-based optically transparent metasurface capable of dual-polarized modulation for electromagnetic stealth. *ACS Appl. Mater. Interfaces* **14**, 31075 (2022).

32. Sun, G., Xing, S. Q., Wang, J. J., Feng, D. J. & Wang, X. S. Flexible conformal multifunctional time-varying phase-modulated metasurface with polarization control for radar feature transformation. *Adv. Opt. Mater.* **12**, 2301743 (2024).

33. Cui, T. J., Qi, M. Q., Wan, X., Zhao, J. & Cheng, Q. Coding metamaterials, digital metamaterials and programmable metamaterials. *Light Sci. Appl.* **3**, e218 (2014).

34. Mnih, V. et al. Human-level control through deep reinforcement learning. *Nature* **518**, 529 (2015).

35. Paszke, A. et al. Pytorch: an imperative style, high-performance deep learning library. In *Proceedings of the 33rd International Conference on Neural Information Processing Systems (NIPS)* (ed. Garnett, R.) 8026–8037 (Curran Associates Inc., 2019)..

36. Li, L. L. et al. Machine-learning reprogrammable metasurface imager. *Nat. Commun.* **10**, 1082 (2019).

37. del Hougne, P., Imani, M. F., Diebold, A. V., Horstmeyer, R. & Smith, D. R. Learned integrated sensing pipeline: reconfigurable metasurface transceivers as trainable physical layer in an artificial neural network. *Adv. Sci.* **7**, 1901913 (2020).

38. Liu, C. et al. A programmable diffractive deep neural network based on a digital-coding metasurface array. *Nat. Electron.* **5**, 113 (2022).

39. Li, S., Liu, Z., Fu, S., Wang, Y. & Xu, F. Intelligent beamforming via physics-inspired neural networks on programmable metasurface. *IEEE Trans. Antennas Propag.* **70**, 4589 (2022).

40. Wen, E., Yang, X. & Sievenpiper, D. F. Real-data-driven real-time reconfigurable microwave reflective surface. *Nat. Commun.* **14**, 7736 (2023).

41. Wang, Z. et al. Multi-task and multi-scale intelligent electromagnetic sensing with distributed multi-frequency reprogrammable metasurfaces. *Adv. Opt. Mater.* **12**, 2203153 (2023).

42. Qian, C. et al. Autonomous aeroamphibious invisibility cloak with stochastic-evolution learning. *Adv. Photonics* **6**, 016001 (2024).

43. Wang, Z. et al. 3D intelligent cloaked vehicle equipped with thousand-level reconfigurable full-polarization metasurfaces. *Adv. Mater.* **36**, 2400797 (2024).

44. Li, W. et al. Intelligent metasurface system for automatic tracking of moving targets and wireless communications based on computer vision. *Nat. Commun.* **14**, 989 (2023).

45. Li, W., Yu, Q., Qiu, J. H. & Qi, J. Intelligent wireless power transfer via a 2-bit compact reconfigurable transmissive-metasurface-based router. *Nat. Commun.* **15**, 2807 (2024).

Acknowledgements

Author contributions

F.L., T.P., and Y.L. conceived the idea, conducted the theoretical analysis, and wrote the manuscript. F.L. and T.P. proposed the design of FISP and built the proof-of-concept prototype system. F.L., W.L., and W.T. designed the adaptive programming algorithm. F.L., W.L., Z.P., D.G., X.J., T.H., and L.W. conducted experiments and data processing. W.T., W.W., M.G., G.Y., L.Z., M.B., and X.W. provided suggestions and comments and helped to organize and revise the draft. All authors discussed the results and contributed to the manuscript.

Competing interests

The authors declare no competing interests.

Additional information

Supplementary information The online version contains supplementary material available at https://doi.org/10.1038/s41467-025-58249-9.

Correspondence and requests for materials should be addressed to Taisong Pan, Wenxuan Tang or Yuan Lin.

Peer review information *Nature Communications* thanks the anonymous reviewer(s) for their contribution to the peer review of this work. A peer review file is available.

Reprints and permissions information is available at http://www.nature.com/reprints